The complementary roles of dynamic contrast-enhanced MRI and [supersript 18]F-fluorodeoxyglucose PET/CT for imaging of carotid atherosclerosis

Citation: Calcagno, Claudia et al. “The Complementary Roles of Dynamic Contrast-Enhanced MRI and 18F-Fluorodeoxyglucose PET/CT for Imaging of Carotid Atherosclerosis.” European Journal of Nuclear Medicine and Molecular Imaging 40.12 (2013): 1884–1893.

Published Version: http://dx.doi.org/10.1007/s00259-013-2518-4

Publisher: Springer Berlin Heidelberg

Permanent Link: http://hdl.handle.net/1721.1/109447

Version: Author's final manuscript: final author’s manuscript post peer review, without publisher’s formatting or copy editing

Eur J Nucl Med Mol Imaging (2013) 40:1884–1893
DOI 10.1007/s00259-013-2518-4

ORIGINAL ARTICLE

The complementary roles of dynamic contrast-enhanced MRI and ^{18}F-fluorodeoxyglucose PET/CT for imaging of carotid atherosclerosis

Claudia Calcagno · Sarayu Ramachandran · David Izquierdo-Garcia · Venkatesh Mani · Antoine Millon · David Rosenbaum · Ahmed Tawakol · Mark Woodward · Jan Bucerius · Erin Moshier · James Godbold · David Kallend · Michael E. Farkouh · Valentin Fuster · James H. F. Rudd · Zahi A. Fayad

Received: 11 April 2013 / Accepted: 11 July 2013 / Published online: 14 August 2013

Abstract
Purpose Inflammation and neovascularization in vulnerable atherosclerotic plaques are key features for severe clinical events. Dynamic contrast-enhanced (DCE) MRI and FDG PET are two noninvasive imaging techniques capable of quantifying plaque neovascularization and inflammatory infiltrate, respectively. However, their mutual role in defining plaque vulnerability and their possible overlap has not been thoroughly investigated. We studied the relationship between DCE-MRI and ^{18}F-FDG PET data from the carotid arteries of 40 subjects

Electronic supplementary material The online version of this article (doi:10.1007/s00259-013-2518-4) contains supplementary material, which is available to authorized users.

C. Calcagno · S. Ramachandran · V. Mani · A. Millon · Z. A. Fayad (✉)
Translational and Molecular Imaging Institute, Mount Sinai School of Medicine, One Gustave L. Levy Place, Box 1234, New York, NY 10029, USA
e-mail: zahi.fayad@mssm.edu

C. Calcagno · S. Ramachandran · V. Mani · A. Millon · Z. A. Fayad
Department of Radiology, Mount Sinai School of Medicine, New York, NY, USA

D. Izquierdo-Garcia
Athinoula A. Martinos Center for Biomedical Imaging, Harvard University - MIT - Massachusetts General Hospital, Charlestown, MA, USA

D. Rosenbaum
Hopital Pitié Salpétrière, Paris, France

A. Tawakol
Harvard Medical School and Massachusetts General Hospital, Boston, MA, USA

M. Woodward
George Institute, University of Sydney, Sydney, Australia

J. Bucerius
Department of Nuclear Medicine, Maastricht University Medical Center, Maastricht, The Netherlands

J. Bucerius
Cardiovascular Research Institute Maastricht (CARIM), Maastricht, The Netherlands

J. Bucerius
Department of Nuclear Medicine, Rheinisch-Westfaelische Technische Hochschule Aachen, Aachen, Germany

E. Moshier · J. Godbold
Biostatistics Shared Research Facility, Mount Sinai School of Medicine, New York, NY, USA

D. Kallend
F. Hoffmann-La Roche Ltd, Basel, Switzerland

M. E. Farkouh · V. Fuster · Z. A. Fayad
Cardiovascular Institute, Mount Sinai School of Medicine, New York, NY, USA

M. E. Farkouh
Peter Munk Cardiac Centre and Li Ka Shing Knowledge Institute, Toronto, Canada

V. Fuster
The Centro Nacional de Investigaciones Cardiovasculares (CNIC), Madrid, Spain

J. H. F. Rudd
Division of Cardiovascular Medicine, University of Cambridge, Cambridge, UK

with coronary heart disease (CHD) or CHD risk equivalent, as a substudy of the dal-PLAQUE trial (NCT00655473).
Methods The dal-PLAQUE trial was a multicenter study that evaluated dalcetrapib, a cholesteryl ester transfer protein modulator. Subjects underwent anatomical MRI, DCE-MRI and ^{18}F-FDG PET. Only baseline imaging and biomarker data (before randomization) from dal-PLAQUE were used as part of this substudy. Our primary goal was to evaluate the relationship between DCE-MRI and ^{18}F-FDG PET data. As secondary endpoints, we evaluated the relationship between (a) PET data and whole-vessel anatomical MRI data, and (b) DCE-MRI and matching anatomical MRI data. All correlations were estimated using a mixed linear model.
Results We found a significant inverse relationship between several perfusion indices by DCE-MRI and ^{18}F-FDG uptake by PET. Regarding our secondary endpoints, there was a significant relationship between plaque burden measured by anatomical MRI with several perfusion indices by DCE-MRI and ^{18}F-FDG uptake by PET. No relationship was found between plaque composition by anatomical MRI and DCE-MRI or ^{18}F-FDG PET metrics.
Conclusion In this study we observed a significant, weak inverse relationship between inflammation measured as ^{18}F-FDG uptake by PET and plaque perfusion by DCE-MRI. Our findings suggest that there may be a complex relationship between plaque inflammation and microvascularization during the different stages of plaque development. ^{18}F-FDG PET and DCE-MRI may have complementary roles in future clinical practice in identifying subjects at high risk of cardiovascular events.

Keywords DCE-MRI · PET/CT · Atherosclerosis · Inflammation · Neovascularization

Introduction

In recent years, significant progress has been made in defining the hallmarks of high-risk, vulnerable atherosclerotic plaques. Vulnerable atheromas are characterized by a large lipid-rich necrotic core (LRNC), thin fibrous cap and prominent inflammatory infiltrate accompanied by abundant and fragile neovessels [1]. This knowledge has stimulated the development of novel, noninvasive imaging techniques to identify vulnerable plaques, with the aim of improving risk stratification, follow-up and management of therapeutic intervention by directly preventing acute events [2]. Techniques such as non-contrast-enhanced, anatomical MRI, CT and ultrasonography can quantify anatomical characteristics and detect key components of vulnerable plaques. Other techniques can extract quantitative information about molecular mechanisms within the plaque. ^{18}F-FDG PET with CT and dynamic contrast-enhanced (DCE) MRI allow measurement of inflammation [3–5] and neovascularization [6–9], respectively, two features of plaque vulnerability. Both techniques show reasonable reproducibility [5, 10] and have been used to track antiatherosclerotic therapies in both clinical and preclinical trials [11–16]. However, the possible degree of overlap of the information provided by each test has not been thoroughly investigated. In this study, we investigated the relationship between ^{18}F-FDG PET/CT and DCE-MRI data from the common carotid arteries of 40 subjects with either coronary heart disease (CHD) or CHD risk factors (CHD risk equivalent) recruited as part of the dal-PLAQUE multicenter trial (NCT00655473) [14, 15].

Methods

Study design

This study was conducted as part of the dal-PLAQUE multicenter trial that evaluated dalcetrapib, a cholesteryl ester transfer protein modulator [14, 15]. The protocol was reviewed and approved by the institutional review board of each participating center. Each participating center was trained in the image acquisition protocol by the core laboratory for image analysis of the dal-PLAQUE trial (Icahn School of Medicine at Mount Sinai, New York, NY). All participants provided written informed consent. Here we report only baseline (prior to randomization) anatomical MRI, DCE-MRI, ^{18}F-FDG PET/CT and biomarker data from the dal-PLAQUE study.

Study population

The study population of dal-PLAQUE comprised patients with CHD or CHD risk equivalent. Patients were clinically stable and receiving appropriate treatment with a statin and/or other drugs for lowering low-density lipoprotein cholesterol (LDL-C) to achieve LDL-C levels of <100 mg/dL (<2.6 mmol/L), unless receiving maximum tolerated doses of therapy or intolerant to statins. From the 189 subjects screened in the dal-PLAQUE trial, 40 were included in this study.

Image acquisition

PET/CT All PET scanners were fully calibrated and corrections applied for attenuation, isotope decay, dead time, normalization, sensitivity, scatter and random coincidences. Patients were instructed to avoid meals rich in carbohydrates starting from 12 h before ^{18}F-FDG injection. Additionally subjects were asked to abstain from heavy physical activity for 24 h before imaging to reduce muscle uptake of ^{18}F-FDG. Approximately 30 min before ^{18}F-FDG injection, glucose was measured: if fasting blood glucose was higher than 200 mg/dL, imaging was rescheduled, otherwise patients were injected with 15 mCi (555 MBq) ^{18}F-FDG, bought commercially from local vendors. After 120 min of FDG circulation time [3–5], a low-dose, non-contrast-enhanced CT scan was performed for attenuation correction and anatomical

coregistration. After aortic imaging for the purpose of the trials, carotid PET data were acquired in 3-D mode for 15 min using one bed position with the superior aspect of the field of view being the internal auditory meatus.

Anatomical MRI Carotid MRI was performed on 1.5-T clinical whole-body systems (Siemens Medical Solutions, Erlangen, Germany) in the head-first supine position using a four-channel carotid array (Machnet, Netherlands) for signal reception. Sixteen non-overlapping cross-sectional T1-weighted (echo time, TE, 9 ms; repetition time, TR, 800 ms), T2-weighted (TE 56 ms; TR 2,000 ms) and proton density-weighted (PD-weighted; TE 9 ms, TR 2,000 ms) images were obtained using multislice, fat-saturated 2-D turbo spin echo (TSE) acquisitions starting at, and extending below, the left carotid bifurcation as previously described [14, 15]. Dark blood was obtained using in-flow and out-flow saturation. Other relevant imaging parameters common to all three acquisitions were: field of view 140×140 mm, matrix size 256×256, in-plane spatial resolution 0.55×0.55 mm, slice thickness 3 mm, interslice gap 0.3 mm, excitation flip angle 90°, refocusing angle 180°, turbo factor 15, four signal averages.

DCE-MRI DCE-MRI was performed on one selected axial slice (chosen from the T1-weighted image set, as the slice with the greatest degree of carotid wall thickening) using a black-blood, fat-saturated TSE sequence after injection of 0.2 mmol/kg gadolinium-diethylene triamine pentaacetic acid (Gd-DTPA, Magnevist; Bayer Schering Pharma) [6]. Black blood was obtained using a double inversion recovery technique. Relevant imaging parameters were: TE 5.6 ms, TR 250 ms, field of view 140×140 mm, matrix size 256×256, in-plane spatial resolution 0.55×0.55 mm, slice thickness 3 mm, excitation flip angle 90°, refocusing angle 180°, turbo factor 15, one signal average, 100 measurements.

More details on the PET and MRI acquisition parameters are provided by Fayad et al. [14, 15]. For the purpose of this comparison, only data from 4 of the 11 imaging sites passed our imaging quality control to ensure uniformity between MRI protocols, vendors and field strength.

Image analysis

A schematic representation of the image analysis is shown in Fig. 1.

Measurement of ^{18}F-FDG uptake PET/CT images were analyzed using OsiriX (Geneva, Switzerland; http://www.osirix-viewer.com/) and in-house software for data handling. Arterial

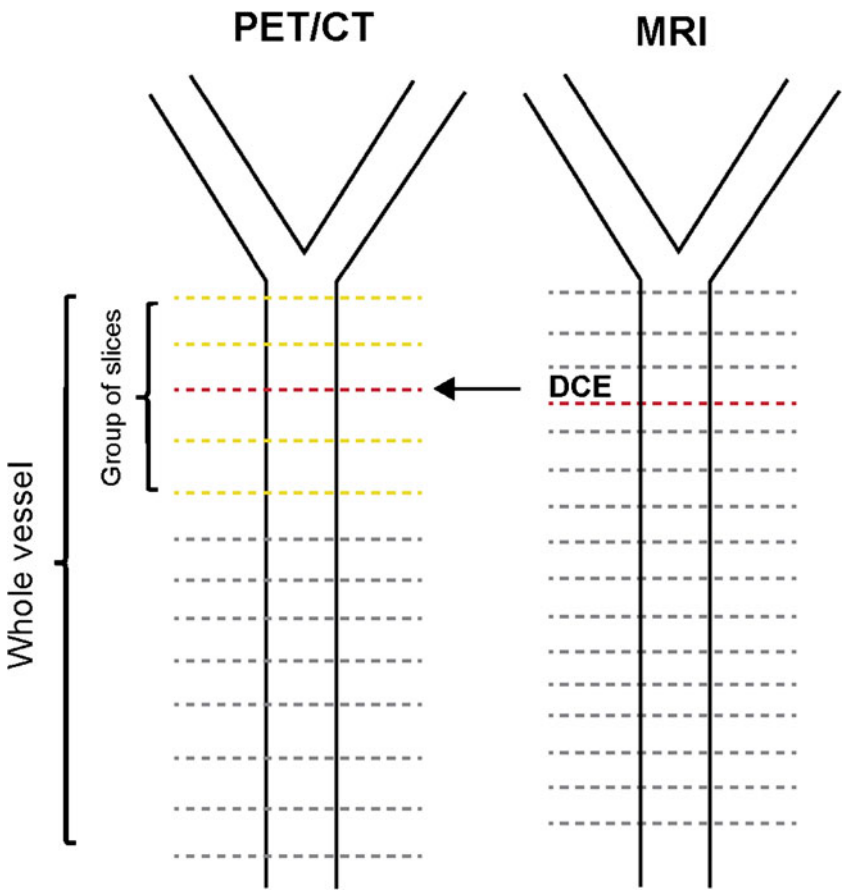

Fig. 1 Schematic view of image analysis in common carotid arteries. *Dashed lines* represent acquired PET/CT and MRI axial slices. Data from all the slices were used for the whole-vessel analyses (*red dashed line* DCE-MRI slice, *orange dashed lines* PET slices surrounding the slice matched with DCE-MRI included in the analysis to take into account possible misregistrations between the two techniques)

^{18}F-FDG uptake was measured by drawing circular regions of interest (ROI) on all PET/CT slices of both common carotid arteries. ROIs were fitted to the artery wall on each axial slice, while coronal and sagittal views were used to ensure that uptake was from the artery. Whole-vessel mean, maximum and mean of maximum standardized uptake values (SUV) were recorded. Arterial SUV was normalized to the blood pool SUV measured from five slices in the jugular vein to calculate the whole-vessel mean, maximum and mean of maximum arterial target-to-background ratio (TBR) [5]. SUV and TBR are both well-validated measures of ^{18}F-FDG uptake. To account for possible misregistration errors between DCE-MRI and PET/CT data, we recorded mean, maximum and mean of maximum SUV and TBR across five slices centered on the slice matching the DCE slice (Fig. 1, approximately 1-cm segment).

Anatomical MRI Inner and outer vessel wall contours were manually traced by an experienced observer on all slices for both common carotid arteries using T2-weighted multislice 2-D TSE images. Mean lumen diameter, vessel diameter, lumen area, wall area, total vessel area, mean wall thickness, standard deviation of wall thickness and normalized wall index for each slice were calculated using a customized software program (Vessel Mass Software; Leiden University Medical Center, The Netherlands) as previously described [17], and interfaced with in-house custom software for data analysis. Whole-vessel parameters were recorded, as well as single slice values matched with DCE-MRI acquisition. Plaque components were classified by an experienced observer by looking simultaneously at the T1-, T2- and PD-weighted multislice 2-D TSE acquisitions to assess the presence or absence of LRNC, calcification and intraplaque hemorrhage, as described by Fayad et al. [14, 15]. Plaques were characterized across the whole vessel as well as on the slice matching with the DCE-MRI acquisition.

DCE-MRI The uptake of contrast agent was evaluated with a custom-made MATLAB (The MathWorks Inc., Natick, MA) program [6]. To ensure proper calibration between different imaging sessions, curves were converted to contrast agent concentrations using the spoiled gradient echo signal model [18] and the widely accepted linear relationship between relaxation rates and concentration. Contrast agent relaxivity was assumed to be 4.3 $mmol^{-1}\ s^{-1}$ [19]. Kinetic modeling was performed using a population arterial input function (AIF) [20] and the model of Tofts et al. with modification [21]. Kinetic parameters v_p (fraction of vascular space), K^{trans} (wash-in constant from plasma to tissue compartment), v_e (fraction of extravascular extracellular space), and K_{ep} (wash-out constant from tissue to plasma compartment) were calculated using standard nonlinear least squares fittings [22] in MATLAB. The non-model based parameter area under the concentration curve (AUC) [6, 10–12] was also calculated at 1 min (AUC1) and 2 min (AUC2) after injection of contrast agent [6] (Fig. 1).

Image coregistration between ^{18}F-FDG PET/CT and DCE-MRI Anatomical coregistration between the DCE-MRI slice and the corresponding PET/CT slice was performed using automated registration of the CT- and PD-weighted high-resolution MR images using a Leonardo workstation (Siemens Medical Solutions, Erlangen, Germany). When necessary, manual adjustments were applied to correct for misalignments in the automated registration.

Statistical methods

The main goal of our analysis was to correlate perfusion metrics by DCE-MRI with plaque inflammation as measured by ^{18}F-FDG PET/CT. We also assessed the correlation between: (a) whole-vessel PET/CT and whole-vessel anatomical MRI variables and (b) single-slice perfusion measures by DCE-MRI with matching single-slice anatomical MRI variables. Correlations were calculated using a mixed linear model with a compound symmetric correlation structure [23], implemented with PROC MIXED in SAS v. 9.2. All data were natural log-transformed to achieve normality. This model accounted for the correlation between measurements of the same variable within each of the 40 patients in the study. The 95 % confidence interval for each correlation coefficient was constructed using the bootstrap method [24], in which 1,000 bootstrap samples of size $n=40$ were generated. Each sample consisted of 40 subjects being sampled with replacement from the complete list of 40 subjects; for each bootstrap sample, PROC MIXED calculated a correlation coefficient from the mixed model. The distribution of these 1,000 correlation coefficients provided estimates of the 2.5th and the 97.5th percentiles as the upper and lower confidence limits for the initial point estimate. When the 95 % confidence interval did not include zero (both limits had the same sign, positive or negative) the correlation was considered significantly different from zero at the 5 % level of significance. To adjust for the multiple statistical tests performed, Bonferroni correction was also applied to the comparisons presented in each table in the Results section. The p value of 0.05 used to establish significance was divided by the number of comparisons considered in each table (36 for Tables 2 and 5; 24 for Table 4). Therefore, $p<0.001$ was required for the comparisons in Tables 2 and 5, and $p<0.02$ was required for the comparisons in Table 4 to reach statistical significance. The results are presented with and without Bonferroni correction. If correlation coefficients were less than 0.3, the correlation was considered weak; if higher or equal to 0.3 but lower than 0.7, the correlation was considered moderate; if higher or equal to 0.7, the correlation was considered strong.

Results

Patient population

The mean age of the population was 64.2 years, and most were men (78.8 %). Baseline lipid biomarkers revealed average total cholesterol of 146.8 mg/dL, with average LDL-C being 74.8 mg/dL and high-density lipoprotein cholesterol (HDL-C) being 45.8 mg/dL. Baseline demographics are presented in Table 1.

Relationship between ^{18}F-FDG PET/CT and DCE-MRI data

The relationship between DCE-MRI and PET variables was analyzed using a mixed linear model (Table 2). Comparing arterial FDG uptake by PET/CT and DCE-MRI measurements without Bonferroni correction, the non-model-based parameter AUC1 showed a weak significant inverse correlation with mean SUV, with a correlation coefficient −0.23. The parameter AUC2 exhibited a weak significant inverse correlation with maximum SUV (correlation coefficient −0.21). The model-based parameter K^{trans}, believed to represent a mixture of flow and permeability, exhibited weak significant inverse correlations with maximum SUV (correlation coefficient −0.22), mean TBR (correlation coefficient −0.24; Fig. 2a) and mean of maximum TBR (correlation coefficient −0.22). The model-based parameter v_p, expressing the fractional plasma volume, showed moderate inverse significant correlations with mean SUV (correlation coefficient −0.41) and mean of maximum SUV (correlation coefficient −0.32). The model-based parameter K_{ep} (backflow constant from tissue to plasma) showed weak inverse significant correlations with mean SUV and TBR (correlation coefficients −0.28 and −0.23; Fig. 2b) and mean of maximum SUV and TBR (correlation coefficients −0.24 and −0.20). The model-based parameter v_e did not show any significant correlations with SUV or TBR values. No significant correlations were found when using Bonferroni correction. Figure 3 shows PET/CT images and DCE-MRI uptake curves from two patients representative of our sample. The PET/CT images and Gd-DTPA uptake data are from a patient with low ^{18}F-FDG uptake by PET/CT but high Gd-DTPA uptake by DCE-MRI (Fig. 3a–c), and a patient with high ^{18}F-FDG and low Gd-DTPA uptake (Fig. 3d–f).

Table 1 Baseline patient characteristics (n = 33)

Characteristic	Value
Age (years), mean (SD)	64 (8.0)
Male sex, *n* (%)	26 (78.8)
Body mass index (kg/m^2), mean (SD)	29 (5.1)
Medical history, *n* (%)	
Type II diabetes	10 (30.3)
Hypertension	20 (60.6)
CHD	28 (84.8)
Abdominal aortic aneurysm	1 (3.0)
Symptomatic carotid disease	3 (9.1)
Peripheral arterial disease	2 (6.1)
Smoking	4 (12.1)
Lipids (mg/dL), mean (SD)	
Total cholesterol	146.8 (29.0)
LDL-C	74.8 (19.8)
HDL-C	45.8 (14.7)
Triglycerides	130.7 (64.1)
High-sensitivity C-reactive protein	2.6 (3.5)

Correlation between anatomical MRI and PET/CT data

Table 3 shows the results of analysis of whole-vessel anatomical MRI data. The dataset was composed mainly of non-complex carotid atherosclerotic plaques, with calcification being identified in only 15.1 % and LRNC in 36.4 % of the lesions. Intraplaque hemorrhage was absent from the entire cohort of subjects in this substudy. Among the slices chosen for DCE-MRI, 6.1 % showed calcification and 18.2 % revealed LRNC. Mean wall thickness averaged across the whole vessel calculated from anatomical MRI data showed a moderate but significant positive correlation with the average whole-vessel TBR, with a correlation coefficient 0.39 (Table 4) without Bonferroni correction. No significant correlations were found between any of the PET variables and plaque composition by MRI (data not shown). No significant correlations were found when using Bonferroni correction.

Correlation between anatomical MRI and DCE-MRI data

Analysis of high-resolution anatomical MRI data revealed that average and standard deviation of wall thickness weakly positively correlated with the DCE-MRI parameter K_{ep} (correlation coefficients 0.21 and 0.25, respectively) when not using Bonferroni correction. No significant correlations were found between DCE-MRI metrics and plaque composition by MRI (data not shown). No significant correlations were found when using Bonferroni correction.

Discussion

The main goal of this study was to investigate the relationship between ^{18}F-FDG PET/CT and DCE-MRI data from the carotid arteries of 40 patients with CHD or CHD risk equivalent recruited as part of the dal-PLAQUE study [14, 15]. These techniques offer a quantitative read-out for plaque macrophages [4] and neovessels, respectively [6, 7], two of the hallmarks of plaque vulnerability. We found a significant weak inverse relationship between the results from the two

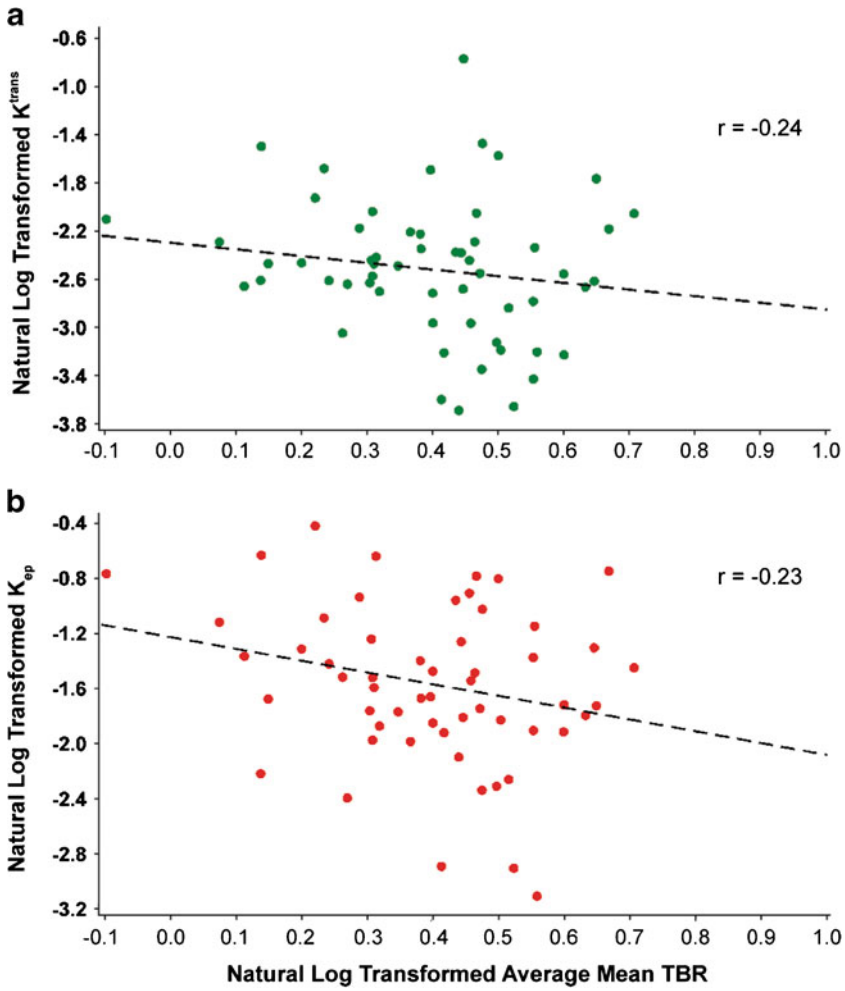

Fig. 2 Correlation between DCE-MRI parameters and mean TBR by PET/CT in the carotid arteries of subjects with CHD or CHD risk equivalent. **a** Correlation between K^{trans} by DCE-MRI and mean TBR by PET/CT. **b** Correlation between K_{ep} by DCE-MRI and mean TBR by PET/CT. *Black dotted line* regression line

techniques. As secondary endpoints, we explored the relationships between non-contrast-enhanced anatomical MRI data and data from both DCE-MRI and FDG PET/CT. The anatomical MRI data showed a significant weak positive correlation with the DCE-MRI data and a significant weak inverse correlation with the PET/CT data.

Previous studies have investigated the relationship between anatomical MRI and ^{18}F-FDG PET/CT data and found higher FDG uptake in complex lesions, but no or only a weak correlation with plaque wall thickness. Silvera et al. found higher FDG uptake in lipid-based compared to collagen-rich or calcified plaques using TBR [25]. Additionally (only in the LRNC group), they found a significant variation in TBR according to the median of the vessel wall thickness. On the contrary, Kwee et al. [26] found higher FDG uptake measured as SUV in fibrous, but not lipid-rich, plaques. Additionally, they found a correlation between SUV and vessel wall volume. In this study, we confirmed a significant relationship between average whole vessel TBR by PET/CT and average wall thickness by anatomical MRI, but fail to demonstrate a correlation between FDG uptake and plaque composition (Table 4). This difference from the two studies mentioned above may be due to the patient population and nature of the lesions (more complex in other studies, versus non-complex in the present study). Additionally, we demonstrates weak but significant correlations between anatomical MRI measures such as average wall area and average and standard deviation of wall thickness and the DCE-MRI metric K_{ep}, while no correlation was found with plaque composition (Table 5).

Recently, Cyran et al. [27] studied the relationship between ^{18}F-FDG PET/CT and DCE-MRI results in patients with supraaortic arteritis, and found a positive significant correlation between mean arterial TBR and extraction fraction of MRI contrast agent. Taqueti et al. [28] also found a positive significant correlation between FDG uptake measured as TBR and K^{trans} by DCE-MRI and neovessels by histology in patients with severe carotid stenosis. In this study we found a weak but significant inverse correlation between model-based and non-model-based DCE-MRI metrics and SUV and TBR by PET/CT. There may be several reasons for this difference in findings. Firstly, it must be noted that the patient populations in the two studies were very different: while Taqueti et al.

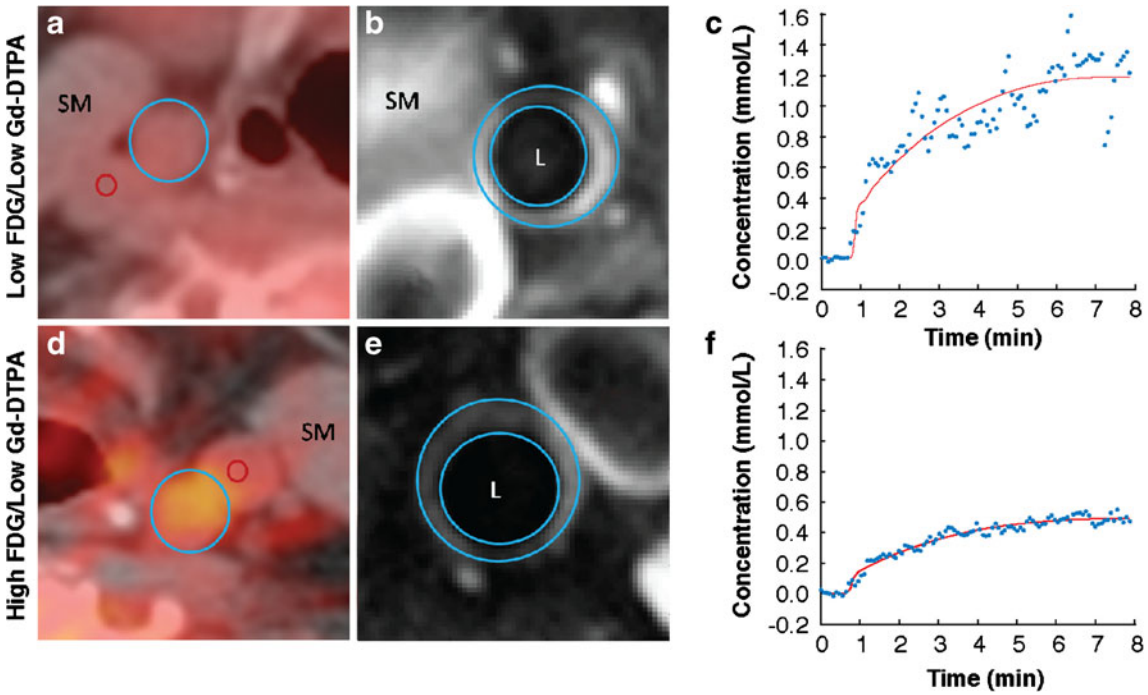

Fig. 3 ^{18}F-FDG PET/CT images and Gd-DTPA uptake data by DCE-MRI from representative patients showing the relationship between Gd-DPTA uptake and ^{18}F-FDG uptake. **a**–**c** Patient with low arterial FDG uptake by PET/CT but high Gd-DTPA uptake by DCE-MRI. **d**–**f** Patient with high arterial FDG uptake by PET/CT but low Gd-DTPA uptake by DCE-MRI. **a**, **d** FDG PET image overlain on CT image (*blue circles* common carotid artery, *red circles* jugular vein). **b**, **e** T1-W MRI image after contrast agent administration. **c**, **f** Kinetic modeling of Gd-DTPA uptake by DCE-MRI (*blue dots* experimental data, *red line* model fit). *SM* skeletal muscle, *L* vessel lumen

[28] studied subjects presenting with a high degree of carotid stenosis, in this study we investigated subjects with non-complex atherosclerotic lesions (Table 3). Differences in medication usage between the population investigated in this study and other studies may also act as a confounding factor. Additionally, while it is known that PET/CT and DCE-MRI provide an indication of the extent of plaque macrophages and neovessels, their metrics may not exclusively reflect these histological features. For example, contrast agent extravasation in DCE-MRI depends not only on neovessel density and permeability, but also on the fractional extravascular extracellular space available for contrast agent distribution [21].

Table 2 Correlation between DCE-MRI and slice-matched ^{18}F-FDG PET/CT parameters (n=40)

PET/CT parameters	DCE-MRI parameters					
	AUC1	AUC2	K^{trans}	v_e	K_{ep}	v_p
SUV_Mean	**−0.23**	−0.22	−0.25	0.02	**−0.28**	**−0.41**
SUV_Max	−0.18	**−0.21**	**−0.22**	−0.04	−0.20	−0.25
SUV_MeanofMax	−0.20	−0.20	−0.22	0.02	**−0.24**	**−0.32**
TBR_Mean	−0.23	−0.20	**−0.24**	−0.02	**−0.23**	−0.30
TBR_Max	−0.10	−0.11	−0.15	−0.14	−0.04	−0.29
TBR_MeanofMax	−0.20	−0.19	**−0.22**	−0.04	**−0.20**	−0.29

Bold type indicates a significant correlation without Bonferroni correction (P<0.05)

Alternatively, it is possible that plaque macrophage content and neovascularization (and therefore ^{18}F-FDG uptake on PET and Gd-DTPA uptake on DCE-MRI) may exhibit different relationships with each other depending on the stage of the plaque that is being imaged.

Another potential explanation for our findings resides in the interplay between neovascularization, hypoxia and inflammation [29]. It is relatively well established that hypoxia and

Table 3 Non-contrast-enhanced MRI analysis

Measure (mean and standard deviation)	Whole vessel (n=33)	DCE-MRI slice (n=40)
Average total vessel area (cm^2), mean (SD)	0.61 (0.20)	0.60 (0.13)
Average wall area (cm^2), mean (SD)	0.28 (0.11)	0.24 (0.06)
Average lumen area (cm^2), mean (SD)	0.32 (0.11)	0.36 (0.08)
Average mean wall thickness (mm), mean (SD)	1.15 (0.24)	0.97 (0.20)
Average standard deviation of wall thickness (mm), mean (SD)	0.27 (0.19)	0.20 (0.11)
Average normalized wall index[a], mean (SD)	0.46 (0.07)	0.40 (0.06)
Calcification, n (%)	5 (15.1)	2 (6.1)
Hemorrhage, n (%)	0 (0)	0 (0)
Lipid rich necrotic core, n (%)	12 (36.4)	6 (18.2)

[a] Wall area/total vessel area based on the average of the right and left carotid arteries

Table 4 Correlation between anatomical MRI and whole-vessel PET/CT data

	Average SUV	Maximum SUV	Average TBR	Maximum TBR
Average total vessel area (cm^2)	0.04	0.00	0.12	0.08
Average wall area (cm^2)	0.05	0.00	0.29	0.23
Average lumen area (cm^2)	0.03	0.01	−0.09	−0.10
Average mean wall thickness (mm)	0.05	0.01	**0.39**	0.33
Average standard deviation of wall thickness (mm)	0.01	−0.03	0.30	0.24
Average normalized wall index	0.04	0.01	0.33	0.29

Bold type indicates a significant correlation without Bonferroni correction ($P<0.05$)

inflammation are intertwined at the molecular, cellular and clinical levels [30]. Hypoxic conditions are known to develop in atherosclerotic plaques as a result of smooth muscle cell proliferation in the tunica intima, subsequent wall thickening, and increased oxygen consumption by macrophages and foam cells [31–33]. Hypoxia induces increased glycolysis [34, 35] in macrophages (hence increased FDG uptake). In addition to increasing macrophage glycolysis, hypoxia is known to increase macrophage activation, phagocytosis [36] and tumor necrosis factor production [37]. This hypothesis offers a possible explanation for our findings, where higher FDG uptake was inversely correlated with plaque neovascularization shown by DCE-MRI. It is therefore possible to envision a scenario where the hypoxia-driven inflammatory response may precede an increase in plaque neovascularization by neoangiogenesis [38]. This hypothesis has been corroborated by more recent in vivo findings by Pedersen et al. [39], which show the relationship between SUV and expression of genes of plaque vulnerability and neoangiogenesis in human carotid specimens. Pedersen et al. found a significant but negative correlation between CD34, a histological marker of microvessel density, and both SUV by ^{18}F-FDG-PET and CD68, a histological marker of macrophages. No correlation was found between SUV and markers of neoangiogenesis (vascular endothelial growth factor). The authors concluded that ^{18}F-FDG uptake inversely reflects microvessel density, but not neoangiogenesis in human atherosclerotic plaques. Since DCE-MRI metrics are known to reflect plaque neovessel content, this may explain the higher substantial ^{18}F-FDG uptake in areas of low uptake of Gd-DTPA on DCE-MRI and vice versa.

Table 5 Correlation between anatomical MRI and DCE-MRI data

	AUC1	AUC2	K^{trans}	v_e	K_{ep}	v_p
Average total vessel area (cm^2)	0.10	0.11	0.09	0.06	0.06	0.12
Average wall area (cm^2)	0.14	0.17	0.15	0.00	0.16	0.09
Average lumen area (cm^2)	0.08	0.07	0.04	0.09	−0.02	0.10
Average mean wall thickness (mm)	0.11	0.14	0.16	−0.05	**0.21**	0.07
Average standard deviation of wall thickness (mm)	0.08	0.08	0.07	−0.21	**0.25**	−0.16
Average normalized wall index	0.07	0.10	0.15	−0.11	0.24	0.00

Bold type indicates a significant correlation without Bonferroni correction ($P<0.05$)

Together with other studies, our findings suggest that ^{18}F-FDG PET and DCE-MRI may offer complementary, non-overlapping information about vascular inflammation and neoangiogenesis. This suggests that these two techniques may be used in combination in future clinical practice for accurate staging and risk stratification of atherosclerotic plaques. However, a more thorough investigation of these two modalities and their underlying histological correlates at the different stages of plaque progression is needed before their clinical use.

Study limitations

Possible limitations of the study are as follows. Firstly, the sample size was relatively small (40 subjects) and comparison of the imaging findings with a histological gold standard was not possible. Due to the small sample size, subgroup analyses of symptomatic versus asymptomatic subjects were also not possible. Secondly, DCE-MRI achieved limited single-slice coverage to maintain sufficiently fast temporal resolution (4.8 s) together with a high spatial resolution (0.5×0.5 mm) for the reliable estimation of contrast agent uptake and good characterization of plaque composition. This required careful matching of DCE-MRI slices with the corresponding anatomical MRI and PET/CT images, which may be affected by misregistration. The development of novel technologies such as integrated PET/MRI scanners will, in the future, allow these studies to be performed simultaneously, naturally providing coregistered PET and MRI images, and therefore eliminating this issue [40]. PET imaging has quite poor spatial resolution for imaging small structures, such as atherosclerotic vessel walls. However, this modality has been used successfully in combination with CT, which provides anatomical details and attenuation correction, to quantify inflammation in atherosclerotic plaques [4]. PET/MRI may allow the application of partial volume correction techniques to help image small structures, such as the vasculature, with increased accuracy [41].

A black-blood sequence was chosen for DCE-MRI acquisition to allow better delineation of these non-complex atherosclerotic lesions from the vessel lumen during dynamic scanning. Despite allowing clear visualization of the arterial vessel wall by suppressing the blood signal, black-blood imaging does not allow sampling a per-patient AIF for kinetic

modeling. A population-derived AIF [20] was used for analysis, which may have introduced inaccuracies into the calculation of model-based parameters. Finally, no significant correlations were found when using Bonferroni correction. While Bonferroni correction is applied when multiple statistical tests are performed to avoid type 1 errors (false positives), it is a rather conservative approach which does increase the chance of type 2 errors (false negatives). While some of the correlations reported without Bonferroni correction are likely to have been false positives, in this case the correction demands $p < 0.001$ (Tables 2 and 5) and $p < 0.002$ (Table 4) to reach significance. As this may conceivably have led to some false negatives, both corrected and uncorrected results are reported.

Conclusion

In conclusion, in this study we found a significant inverse relationship between non-model and model-based perfusion indices by DCE-MRI (indices of neovascularization) and SUV and TBR by PET/CT (markers of macrophage content). This finding, in combination with other findings in the literature, suggests that there may be a complex relationship between plaque inflammation and neovascularization, and that ^{18}F-FDG PET and DCE-MRI images have complex histological correlates, whose relationship may change during plaque progression. The combination of PET/CT and DCE-MRI imaging may prove to be a useful tool in drug development for proof of concept of new therapies.

Acknowledgments F. Hoffmann-La Roche Ltd funded the dal-PLAQUE study and provided third-party editorial support, through Prime Healthcare Ltd, for the preparation of the manuscript. C.C. acknowledges grant and research support from the National Institutes of Health and National Heart Lung and Blood Institute (NIH/NHLBI R01 HL071021, NIH/NHLBI R01 HL078667 and NIH/NCRR UL1RR029887).

Conflicts of interest S.R., D.I.-G., A.M., D.R., J.B., E.M., J.G. and V.F. indicate that they have nothing to disclose. VM discloses that he receives consulting fees from Tursiop Inc. A.T. discloses that he has received honoraria from Roche, BMS and Novartis, and research grants from Merck, BMS, Genentech, GSK and VBL. M.W. discloses that he has received honoraria from Roche. D.K. is an employee of F. Hoffmann-La Roche Ltd. M.E.F. discloses that he has received honoraria from Roche and acted as a consultant to Genentech. J.H.F.R. discloses that he has received honoraria from Roche and is part-supported by the National Institute for Health Research Cambridge Biomedical Research Centre. Z.A.F. discloses that he has received research grants from Roche, GlaxoSmithKline, Merck, VBL Therapeutics, Novartis, Bristol-Myers Squibb, and Via Pharmaceuticals, and honoraria from Roche.

References

1. Virmani R, Burke AP, Farb A, Kolodgie FD. Pathology of the vulnerable plaque. J Am Coll Cardiol. 2006;47 Suppl:C13–8.
2. Fuster V, Fayad ZA, Moreno PR, Poon M, Corti R, Badimon JJ. Atherothrombosis and high-risk plaque: Part II: approaches by noninvasive computed tomographic/magnetic resonance imaging. J Am Coll Cardiol. 2005;46:1209–18.
3. Rudd JH, Warburton EA, Fryer TD, Jones HA, Clark JC, Antoun N, et al. Imaging atherosclerotic plaque inflammation with [18F]-fluorodeoxyglucose positron emission tomography. Circulation. 2002;105:2708–11.
4. Tawakol A, Migrino RQ, Bashian GG, Bedri S, Vermylen D, Cury RC, et al. In vivo 18F-fluorodeoxyglucose positron emission tomography imaging provides a noninvasive measure of carotid plaque inflammation in patients. J Am Coll Cardiol. 2006;48:1818–24.
5. Rudd JH, Myers KS, Bansilal S, Machac J, Rafique A, Farkouh M, et al. [18]Fluorodeoxyglucose positron emission tomography imaging of atherosclerotic plaque inflammation is highly reproducible: implications for atherosclerosis therapy trials. J Am Coll Cardiol. 2007;50:892–6.
6. Calcagno C, Cornily JC, Hyafil F, Rudd JH, Briley-Saebo KC, Mani V, et al. Detection of neovessels in atherosclerotic plaques of rabbits using dynamic contrast enhanced MRI and 18F-FDG PET. Arterioscler Thromb Vasc Biol. 2008;28:1311–7.
7. Kerwin W, Hooker A, Spilker M, Vicini P, Ferguson M, Hatsukami T, et al. Quantitative magnetic resonance imaging analysis of neovasculature volume in carotid atherosclerotic plaque. Circulation. 2003;107:851–6.
8. Kerwin WS, O'Brien KD, Ferguson MS, Polissar N, Hatsukami TS, Yuan C. Inflammation in carotid atherosclerotic plaque: a dynamic contrast-enhanced MR imaging study. Radiology. 2006;241:459–68.
9. Kerwin WS, Oikawa M, Yuan C, Jarvik GP, Hatsukami TS. MR imaging of adventitial vasa vasorum in carotid atherosclerosis. Magn Reson Med. 2008;59:507–14.
10. Calcagno C, Vucic E, Mani V, Goldschlager G, Fayad ZA. Reproducibility of black blood dynamic contrast-enhanced magnetic resonance imaging in aortic plaques of atherosclerotic rabbits. J Magn Reson Imaging. 2010;32:191–8.
11. Lobatto ME, Fayad ZA, Silvera S, Vucic E, Calcagno C, Mani V, et al. Multimodal clinical imaging to longitudinally assess a nanomedical anti-inflammatory treatment in experimental atherosclerosis. Mol Pharm. 2010;7:2020–9.
12. Vucic E, Dickson SD, Calcagno C, Rudd JH, Moshier E, Hayashi K, et al. Pioglitazone modulates vascular inflammation in atherosclerotic rabbits noninvasive assessment with FDG-PET-CT and dynamic contrast-enhanced MR imaging. JACC Cardiovasc Imaging. 2011;4:1100–9.
13. Vucic E, Calcagno C, Dickson SD, Rudd JH, Hayashi K, Bucerius J, et al. Regression of inflammation in atherosclerosis by the LXR agonist R211945: a noninvasive assessment and comparison with atorvastatin. JACC Cardiovasc Imaging. 2012;5:819–28.
14. Fayad ZA, Mani V, Woodward M, Kallend D, Bansilal S, Pozza J, et al. Rationale and design of dal-PLAQUE: a study assessing efficacy and safety of dalcetrapib on progression or regression of atherosclerosis using magnetic resonance imaging and 18F-fluorodeoxyglucose positron emission tomography/computed tomography. Am Heart J. 2011;162:214–221.e2.
15. Fayad ZA, Mani V, Woodward M, Kallend D, Abt M, Burgess T, et al. Safety and efficacy of dalcetrapib on atherosclerotic disease using novel non-invasive multimodality imaging (dal-PLAQUE): a randomised clinical trial. Lancet. 2011;378:1547–59.
16. Fayad ZA, Mani V, Fuster V. The time has come for clinical cardiovascular trials with plaque characterization as an endpoint. Eur Heart J. 2012;33:160–1.
17. Mani V, Muntner P, Gidding SS, Aguiar SH, El Aidi H, Weinshelbaum KB, et al. Cardiovascular magnetic resonance parameters of atherosclerotic plaque burden improve discrimination of prior major adverse cardiovascular events. J Cardiovasc Magn Reson. 2009;11:10.
18. Haacke EM, Brown RW, Thompson MR, Venkatesan R. Magnetic resonance imaging: physical principles and sequence design. New York: Wiley; 1999.

19. Sasaki M, Shibata E, Kanbara Y, Ehara S. Enhancement effects and relaxivities of gadolinium-DTPA at 1.5 versus 3 Tesla: a phantom study. Magn Reson Med Sci. 2005;4:145–9.
20. Parker GJ, Roberts C, Macdonald A, Buonaccorsi GA, Cheung S, Buckley DL, et al. Experimentally-derived functional form for a population-averaged high-temporal-resolution arterial input function for dynamic contrast-enhanced MRI. Magn Reson Med. 2006;56:993–1000.
21. Tofts PS, Brix G, Buckley DL, Evelhoch JL, Henderson E, Knopp MV, et al. Estimating kinetic parameters from dynamic contrast-enhanced T(1)-weighted MRI of a diffusable tracer: standardized quantities and symbols. J Magn Reson Imaging. 1999;10:223–32.
22. Murase K. Efficient method for calculating kinetic parameters using T1-weighted dynamic contrast-enhanced magnetic resonance imaging. Magn Reson Med. 2004;51:858–62.
23. Hamlett A, Ryan L, Wolfinger R. On the use of PROC MIXED to estimate correlation in the presence of repeated measures. Proceedings of the Twenty-Ninth Annual SAS Users Group International Conference. Cary, NC: SAS Institute Inc.; 2004. paper 198-29.
24. Efron B, Tibshirani RJ. An introduction to the bootstrap. New York: Chapman & Hall; 1993.
25. Silvera SS, Aidi HE, Rudd JH, Mani V, Yang L, Farkouh M, et al. Multimodality imaging of atherosclerotic plaque activity and composition using FDG-PET/CT and MRI in carotid and femoral arteries. Atherosclerosis. 2009;207:139–43.
26. Kwee RM, Teule GJ, van Oostenbrugge RJ, Mess WH, Prins MH, van der Geest RJ, et al. Multimodality imaging of carotid artery plaques: 18F-fluoro-2-deoxyglucose positron emission tomography, computed tomography, and magnetic resonance imaging. Stroke. 2009;40:3718–24.
27. Cyran CC, Sourbron S, Bochmann K, Habs M, Pfefferkorn T, Rominger A, et al. Quantification of supra-aortic arterial wall inflammation in patients with arteritis using high resolution dynamic contrast-enhanced magnetic resonance imaging: initial results in correlation to [18F]-FDG PET/CT. Invest Radiol. 2011;46:594–9.
28. Taqueti V, Carli MD, Jerosch-Herold M, Sukhova G, Murthy V, Folco E, et al. Increased microvascular blood flow and permeability associates with FDG signal in human atheroma. J Am Coll Cardiol. 2012;59(13):E1309.
29. Minchenko A, Leshchinsky I, Opentanova I, Sang N, Srinivas V, Armstead V, et al. Hypoxia-inducible factor-1-mediated expression of the 6-phosphofructo-2-kinase/fructose-2,6-bisphosphatase-3 (PFKFB3) gene. Its possible role in the Warburg effect. J Biol Chem. 2002;277:6183–7.
30. Eltzschig HK, Carmeliet P. Hypoxia and inflammation. N Engl J Med. 2011;364:656–65.
31. Moreno PR, Purushothaman KR, Fuster V, Echeverri D, Truszczynska H, Sharma SK, et al. Plaque neovascularization is increased in ruptured atherosclerotic lesions of human aorta: implications for plaque vulnerability. Circulation. 2004;110:2032–8.
32. Fuster V, Moreno PR, Fayad ZA, Corti R, Badimon JJ. Atherothrombosis and high-risk plaque: part I: evolving concepts. J Am Coll Cardiol. 2005;46:937–54.
33. Ribatti D, Levi-Schaffer F, Kovanen PT. Inflammatory angiogenesis in atherogenesis – a double-edged sword. Ann Med. 2008;40:606–21.
34. Folco EJ, Sheikine Y, Rocha VZ, Christen T, Shvartz E, Sukhova GK, et al. Hypoxia but not inflammation augments glucose uptake in human macrophages: implications for imaging atherosclerosis with 18fluorine-labeled 2-deoxy-D-glucose positron emission tomography. J Am Coll Cardiol. 2011;58:603–14.
35. Kawaguchi T, Veech RL, Uyeda K. Regulation of energy metabolism in macrophages during hypoxia. Roles of fructose 2,6-bisphosphate and ribose 1,5-bisphosphate. J Biol Chem. 2001;276:28554–61.
36. Anand RJ, Gribar SC, Li J, Kohler JW, Branca MF, Dubowski T, et al. Hypoxia causes an increase in phagocytosis by macrophages in a HIF-1alpha-dependent manner. J Leukoc Biol. 2007;82:1257–65.
37. Leeper-Woodford SK, Detmer K. Acute hypoxia increases alveolar macrophage tumor necrosis factor activity and alters NF-kappaB expression. Am J Physiol. 1999;276:L909–16.
38. Moulton KS. Angiogenesis in atherosclerosis: gathering evidence beyond speculation. Curr Opin Lipidol. 2006;17:548–55.
39. Pedersen SF, Graebe M, Hag AM, Hoejgaard L, Sillesen H, Kjaer A. Microvessel density but not neoangiogenesis is associated with 18F-FDG uptake in human atherosclerotic carotid plaques. Mol Imaging Biol. 2012;14:384–92.
40. Yankeelov TE, Peterson TE, Abramson RG, Izquierdo-Garcia D, Arlinghaus LR, Li X, et al. Simultaneous PET-MRI in oncology: a solution looking for a problem? Magn Reson Imaging. 2012;30:1342–56.
41. Torigian DA, Zaidi H, Kwee TC, Saboury B, Udupa JK, Cho ZH, et al. PET/MR imaging: technical aspects and potential clinical applications. Radiology. 2013;267:26–44.